

# Spectral Mixture Analysis of Hyperspectral Scenes Using Intelligently Selected Training Samples

Javier Plaza and Antonio Plaza, *Senior Member, IEEE*

**Abstract**—In this letter, we address the use of artificial neural networks for spectral mixture analysis of hyperspectral scenes. We specifically focus on the issue of how to effectively train neural network architectures in the context of spectral mixture analysis applications. To address this issue, a multilayer perceptron neural architecture is combined with techniques for intelligent selection and labeling of training samples directly obtained from the input data, thus maximizing the information that can be obtained from those samples while reducing the need for *a priori* information about the scene. The proposed approach is compared to unconstrained and fully constrained linear mixture models using hyperspectral data sets acquired (in the laboratory) from artificial forest scenes, using the compact airborne spectrographic imaging system. The Spreading of Photons for Radiation INTerception (SPRINT) canopy model, which assumes detailed knowledge about object geometry, was employed to evaluate the results obtained by the different methods. Our results show that the proposed approach, when trained with both pure and mixed training samples (generated automatically without *prior* information) can provide similar results to those provided by SPRINT, using very few labeled training samples. An application to real airborne data using a set of hyperspectral images collected at different altitudes by the digital airborne imaging spectrometer 7915 and the reflective optics system imaging spectrometer, operating simultaneously at multiple spatial resolutions, is also presented and discussed.

**Index Terms**—Hyperspectral imaging, intelligent training, neural networks, spectral mixture analysis.

## I. INTRODUCTION

MOST of the pixels collected by hyperspectral imaging instruments contain the resultant mixed spectra from the reflected surface radiation of various subpixel constituent materials [1]. Mixed pixels exist for several reasons. First, if the spatial resolution of the sensor is not fine enough to separate different pure signature classes at a macroscopic level, these can jointly occupy a single pixel, and the resulting spectral measurement will be a composite of the individual pure spectra, often called *endmembers* in hyperspectral analysis terminology [2]. Second, mixed pixels can also result when distinct materials are combined into a homogeneous or intimate mixture, and this circumstance occurs independently of the spatial resolution of the sensor [3].

A standard approach to characterize mixed pixels in the literature has been linear spectral unmixing, which involves

Manuscript received April 9, 2009; revised August 10, 2009 and September 28, 2009. Date of publication December 4, 2009; date of current version April 14, 2010.

The authors are with the Department of Technology of Computers and Communications, University of Extremadura, Cáceres 10071, Spain.

Color versions of one or more of the figures in this paper are available online at <http://ieeexplore.ieee.org>.

Digital Object Identifier 10.1109/LGRS.2009.2036139

the separation of a pixel spectrum into its pure component endmember spectra, and the estimation of the abundance value for each endmember in the pixel [2]. The linear model assumes minimal secondary reflections and/or multiple scattering effects in the data collection procedure. The resulting mixed spectrum can be expressed as a linear combination of endmember components, weighted by a scalar endmember abundance fraction as follows:

$$\mathbf{r} = \mathbf{E}\mathbf{a} + \mathbf{n} = \sum_{i=1}^p \mathbf{e}_i a_i + \mathbf{n} \quad (1)$$

where  $\mathbf{r} = [r_1, r_2, \dots, r_N]^T$  is an  $N$ -dimensional pixel vector given by a collection of values at different wavelengths,  $\mathbf{E}$  is a matrix containing  $p$  endmember signatures, i.e.,  $\mathbf{E} = \{\mathbf{e}_i\}_{i=1}^p$ ,  $\mathbf{a}$  is a vector containing the fractional abundance values for each of the  $p$  endmembers in  $\mathbf{r}$ , i.e.,  $\mathbf{a} = [a_1, a_2, \dots, a_p]^T$ , and  $\mathbf{n}$  is a noise vector. Two constraints are generally imposed into the linear mixture model above: the abundance-sum-to-one constraint, i.e.,  $\sum_{i=1}^p a_i = 1$ , and the abundance nonnegativity constraint, i.e.,  $a_i \geq 0$  for all  $1 \leq i \leq p$  [4].

Although the linear mixture model has practical advantages such as ease of implementation and flexibility in different applications [5], there are many naturally occurring situations where nonlinear models may best characterize the resultant mixed spectra for certain endmember distributions [6], [7]. In those cases, the mixed spectra are better described by assuming that part of the source radiation is multiply scattered before being collected at the sensor [3]. A general expression for the nonlinear mixture model can be given as  $\mathbf{r} = f(\mathbf{E}, \mathbf{a}) + \mathbf{n}$ , where  $f$  is an unknown nonlinear function that defines the interaction between  $\mathbf{E}$  and  $\mathbf{a}$ . Although the use of nonlinear physical models has been quite popular in the characterization of spectral mixtures based on *prior* knowledge [8], [9], fewer efforts have been devoted to designing data sampling techniques able to estimate  $f$ .

In this letter, we focus on the use of artificial neural networks (ANNs) to accomplish the aforementioned task. We hypothesize that the problem of mixed pixel characterization using ANNs demands intelligent training algorithms able to automatically label the most informative training samples, thus optimizing the compromise between estimation accuracy (to be maximized) and ground-truth knowledge (to be minimized). To address this issue, we develop an unsupervised algorithm for intelligent selection and labeling of *informative* training samples, which are used to train a feedforward ANN of various layers: the multilayer perceptron (MLP) [10], which has been often used in the past to decompose mixed pixels [11], [12]. The proposed approach is investigated and compared to fully constrained and unconstrained linear mixture models

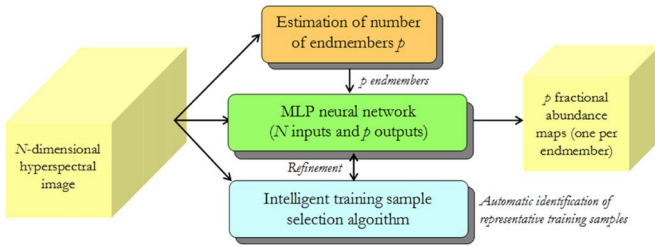


Fig. 1. Neural network-based spectral unmixing architecture.

using data acquired in the laboratory from artificial scenes using a Compact Airborne Spectrographic Imaging (CASI) instrument [13] and real airborne hyperspectral scenes collected by the Digital Airborne Imaging Spectrometer (DAIS) 7915 and Reflective Optics System Imaging Spectrometer (ROSIS) sensors. The Spreading of Photons for Radiation INTerception (SPRINT) model [9] and a combination of multiple resolution airborne data and ground measurements are, respectively, used in experiments for validation purposes.

## II. NEURAL NETWORK-BASED SPECTRAL UNMIXING

Fig. 1 shows a schematic block diagram of the proposed neural network-based unmixing architecture. The first step consists of an estimation of the number of endmembers  $p$  in the input data. For this purpose, in this letter, we use the concept of virtual dimensionality [14]. Then, a supervised MLP neural network is trained with intelligently selected training samples (both pure and mixed) in order to estimate endmember fractional abundances. The number of neurons at the input layer of the MLP architecture equals the number of spectral bands  $N$ . The training samples are labeled pixel vectors directly obtained from the hyperspectral data, with no previous dimensionality reduction. The second layer is the hidden layer, and the third layer is the output layer. The number of neurons at the output layer  $p$  equals the number of estimated endmembers. It should be noted that the number of hidden neurons in the MLP architecture can be fine tuned depending on the problem under consideration [10]. However, in this letter, we are mainly interested in exploring training mechanisms and their implications, without particular emphasis on careful adjustment of neural network configuration parameters. Subsequently, finding optimal parameters for the hidden layer is beyond our scope. Based on previous results in the literature and our own experimentation, we have considered one hidden layer only, with the number of neurons empirically set to the square root of the product of the number of input features and information classes, a configuration that has been shown to be successful for MLP-based mixed pixel characterization in previous work [7]. It is also worth noting that our training algorithm uses Bayesian inference techniques [15] to select the values of regularization coefficients using only the training data. This approach avoids overfitting issues but may include some training error resulting from the fact that training and testing data are mixed together. However, regularization is used in this letter instead of cross-validation mainly due to the deterministic nature of our proposed approach for selection of training samples. This also comes at the expense of increasing the complexity of the learning stage [15].

## III. AUTOMATIC SELECTION OF TRAINING SAMPLES

The quality of training has a significant effect on mixed pixel characterization using neural networks [16]. Conventional approaches for selection of training samples often perform this task randomly, or by choosing the samples located in exemplar regions of each class only, while atypical cases are often removed or down-weighted in training set refinement operations. Such exemplar training patterns are located near the central *core* of the class in feature space. However, a key concern in the context of mixed pixel interpretation is how to identify and characterize the response of sites that lie away from the class core, and near to the decision boundaries commonly used in conventional full-pixel classification. Therefore, *border* [17] (or, equivalently, *mixed*) training samples may be useful to refine a set of fractional abundance estimations obtained by using only spectrally pure training samples.

In this section, we describe a new technique for automatic selection and labeling of training samples from the input hyperspectral data. The proposed technique, called mixed training algorithm (MTA), first uses Winter's N-FINDER algorithm [18] as an approach to automatically label spectrally pure training samples (endmembers) without prior knowledge. Then, it iteratively seeks for the most highly mixed pixels in the input data set by following a procedure which behaves in an opposite way as N-FINDER and other convex geometry-based endmember extraction methods [2], i.e., it automatically selects and labels highly mixed training samples. Different sets of training samples, obtained by the MTA discussed in this section, will be used in the following section to investigate the impact of the composition of the training set on the characterization of mixed pixels. The MTA can be summarized by the following steps.

- 1) Use the N-FINDER algorithm to produce an initial set of  $p$  pure training samples (endmembers) which are labeled by assuming that the vector of fractional abundances associated to each extracted endmember  $s_i$  is formed by  $\hat{a}_i = 1.0$  (meaning 100% abundance), and  $\hat{a}_j = 0.0$  (meaning 0% abundance) for  $j \neq i$ , with  $1 \leq j \leq p$ .
- 2) Compute  $c_p = (1/p) \sum_{i=1}^p s_i$ , i.e., the centroid of the simplex defined by the set of spectral endmembers  $\{s_i\}_{i=1}^p$  produced for the input hyperspectral scene by the N-FINDER algorithm.
- 3) At iteration  $j \geq 1$ , calculate a pointwise spectral *distance* between each pixel vector  $r$  in the input hyperspectral data and  $c_p$ , and mark the pixel vector which provides the lowest *distance* value (i.e., the most spectrally similar to  $c_p$ ) as a new training sample  $t_j$ .
- 4) Label the training sample  $t_j$  by obtaining a vector of fractional estimates  $a_j = [\hat{a}_1, \hat{a}_2, \dots, \hat{a}_p]^T$  in which

$$\hat{a}_i = \frac{\text{distance}(t_j, s_i)}{\sum_{i=1}^p \text{distance}(t_j, s_i)}, \quad \text{with } 1 \leq i \leq p. \quad (2)$$

- 5) Remove the pixel previously selected as a training sample from the input hyperspectral scene and repeat from step 3 until a final set of  $k$  mixed labeled training samples  $\{t_j\}_{j=1}^k$  is generated. Each pair formed by a labeled training sample  $t_j$  and its associated vector of fractional abundances  $a_j$ , estimated by means of (2), is used to train the proposed MLP-based neural network.

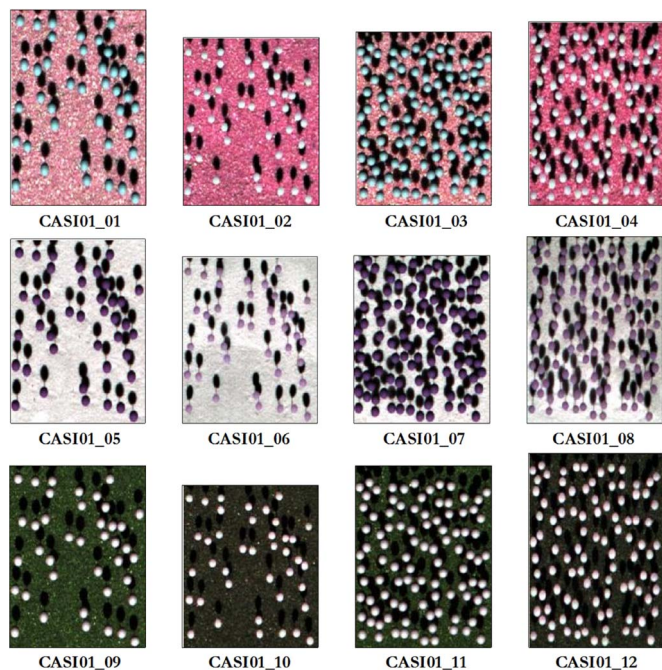


Fig. 2. Color images of the CASI laboratory scenes formed using band 50 (770 nm) as red, band 30 (618 nm) as green, and band 20 (543 nm) as blue.

It should be noted that the MTA was implemented using the spectral angle distance (SAD) [3] as the baseline metric.

#### IV. RESULTS USING LABORATORY DATA

The CASI scenes used in experiments were obtained by the following procedure [13]. Two kinds of objects, namely, opaque and translucent, were mounted on stems to simulate forest crowns on trunks. These simulated “trees” were randomly placed on a mounting board covered with one of the three backgrounds: dark, green, and white. The dimensions of tree crowns for opaque and translucent trees ranged from 1.3 to 1.7 cm. Canopies of both opaque and translucent trees were designed with sparse and dense populations. For the sparse population, 40 trees were planted in an area of 40 cm by 40 cm, while 100 trees were planted in the same area for the dense population. The scene illumination in this simulation was generated using a 100-W tungsten lamp and illumination angle of 40°. Twelve hyperspectral images (labeled as CASI01\_01 to CASI01\_12) were acquired by CASI [13], a pushbroom imager, by moving the entire scene perpendicularly at a constant rate with respect to the CASI field of view. The scenes (see Fig. 2) were acquired in 72 spectral channels covering the spectral region from 414 to 914 nm, at nominal spectral resolution of 7.5 nm. The spatial resolution in the direction of across track is 0.27 cm. The spectral signatures of the  $p = 3$  endmembers extracted by the N-FINDR algorithm from the scenes with sparse opaque trees are shown in Fig. 3.

Table I shows the endmember fractional abundances estimated by the unconstrained (UCLSU) and fully constrained (FCLSU) linear spectral unmixing algorithms described in [4], and by the proposed MLP-based architecture trained using: 1) only the samples labeled by N-FINDR; 2) the samples labeled by N-FINDR plus MTA; and 3) randomly generated training samples. In the first case, only  $p = 3$  pure samples

labeled by N-FINDR were used to train the MLP architecture. In the second case, the training set was expanded by including  $k = 4$  additional mixed training samples labeled by MTA. In this case, we tested values in the range  $k = \{1, \dots, 20\}$  and experimentally observed that values of  $k < 3$  resulted in less accurate fractional abundance estimation results (comparable to those produced by UCLSU and FCLSU), while values of  $k > 5$  did not significantly improve the quality of abundance estimations. Finally, in the third case, we adopted a random training sample selection algorithm using (2) to label each randomly selected training sample, and varied  $k$  in the range  $\{1, \dots, 20\}$ . In this case, we conducted ten Monte Carlo runs for each value of  $k$  and reported in Table I only the best mean scores for each scene, generally obtained for  $k = 20$ . In all experiments, the quality of fractional abundances was assessed using the abundance estimations provided by the SPRINT canopy model (also reported in the Table I). The most similar fractional abundance estimations across all tested methods with regard to SPRINT are shown in bold typeface. In order to interpret the results in Table I, let us first focus on the scenes with opaque trees and sparse population. The errors in the fractions of the endmembers obtained by FCLSU and UCLSU are larger for the scene with white background than for the scenes with dark and green background. This is because, in the scene with white background, the high reflectance of the background increases the multiple scattering between tree crowns and the background. It can also be seen from Table I that the proposed intelligently trained MLP (using  $p = 3$  endmembers plus  $k = 4$  training samples) generally provided the most similar abundance estimation results with regard to the SPRINT canopy model, in particular, for the scene with white background. For illustrative purposes, Fig. 4 shows the abundance maps for the sunlit tree, background, and shadow endmembers obtained after applying the proposed method to this particular scene (CASI01\_05). When the MLP was trained using randomly selected training samples, the fractional abundance estimates could not generally improve those obtained using the other tested methods, despite the higher number of labeled training samples used for the learning stage. For the scenes with translucent trees and sparse population, the fractions of the endmembers estimated by the intelligently trained MLP were also the most similar to those reported by the SPRINT model. A comparison of the estimations provided by FCLSU (and particularly UCLSU) for the scenes with translucent trees with those obtained for the scenes with opaque trees reveals that the errors in the estimated fractions are generally larger for the scenes with translucent trees. This is likely due to the relative increase in multiple scattering between crowns and the background due to crown transparency. For the scenes with opaque trees and dense population, the FCLSU and UCLSU estimation errors for the scene with white background are increased compared with the scenes with dark and green background. If we compare these results with the estimations provided for the scenes with sparse population, we can observe that the abundance estimation errors increase. This is because, for the dense canopies, the multiple scattering between tree crowns and the background is larger. Here, the intelligently trained MLP again provided the most similar estimations with regard to those provided by the SPRINT model, followed by the MLP trained with a comparatively higher number of randomly selected samples. Finally, for the scenes with translucent trees

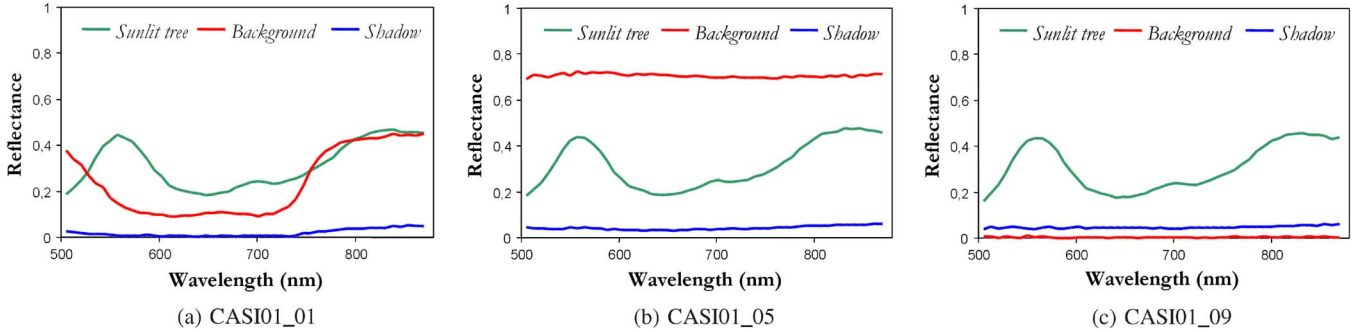


Fig. 3. Endmember spectra for sunlit tree, background, and shadow in selected CASI scenes with (a) green, (b) white, and (c) dark background.

TABLE I  
FRACTIONAL ABUNDANCE ESTIMATIONS PROVIDED BY DIFFERENT SPECTRAL MIXTURE ANALYSIS METHODS FOR THE MAIN CONSTITUENTS IN THE CASI SCENES. THE MOST SIMILAR ESTIMATIONS WITH REGARDS TO THE SPRINT CANOPY MODEL ARE SHOWN IN BOLD TYPEFACE

Scene	Endmember	FCLSU	UCLSU	MLP (Random)	MLP (N-FINDR)	MLP (MTA)	SPRINT
CASI01_01 (sparse, opaque trees, green background)	Sunlit tree	0.083	0.101	0.062	0.095	<b>0.105</b>	0.109
	Background	0.727	0.728	0.841	<b>0.724</b>	0.735	0.723
	Shadow	0.189	0.175	0.096	0.180	<b>0.166</b>	0.167
	Total	1.000	1.004	0.999	0.999	1.006	0.999
CASI01_02 (sparse, transl. trees, green background)	Sunlit tree	0.074	0.084	0.048	0.073	<b>0.086</b>	0.104
	Background	0.805	0.801	0.863	0.746	<b>0.722</b>	0.701
	Shadow	0.120	0.103	0.088	0.180	<b>0.191</b>	0.194
	Total	1.000	0.998	0.999	0.999	0.999	0.999
CASI01_03 (dense, opaque trees, green background)	Sunlit tree	0.183	0.205	0.207	0.232	<b>0.283</b>	0.294
	Background	<b>0.404</b>	0.433	0.516	0.457	0.409	0.383
	Shadow	0.413	0.352	0.276	<b>0.311</b>	0.307	0.318
	Total	1.000	0.990	0.999	1.000	0.999	0.995
CASI01_04 (dense, transl. trees, green background)	Sunlit tree	0.181	0.195	0.150	0.178	<b>0.264</b>	0.279
	Background	0.547	0.489	0.675	0.567	<b>0.349</b>	0.357
	Shadow	0.272	0.311	0.175	0.253	<b>0.387</b>	0.362
	Total	1.000	0.995	1.000	0.998	1.000	0.998
CASI01_05 (sparse, opaque trees, white background)	Sunlit tree	0.074	0.067	0.120	0.127	<b>0.115</b>	0.109
	Background	0.655	0.620	0.606	0.609	<b>0.710</b>	0.723
	Shadow	0.271	0.223	0.273	0.264	<b>0.173</b>	0.167
	Total	1.000	0.910	0.999	1.000	0.998	0.999
CASI01_06 (sparse, transl. trees, white background)	Sunlit tree	<b>0.105</b>	0.026	0.631	0.129	0.090	0.104
	Background	0.796	0.789	0.342	0.464	<b>0.737</b>	0.701
	Shadow	0.099	0.170	0.025	0.407	<b>0.172</b>	0.194
	Total	1.000	0.985	0.998	1.000	0.999	0.999
CASI01_07 (dense, opaque trees, white background)	Sunlit tree	0.204	0.190	0.370	0.315	<b>0.290</b>	0.294
	Background	0.429	0.400	0.462	0.445	<b>0.377</b>	0.383
	Shadow	0.367	0.422	0.176	0.240	<b>0.335</b>	0.318
	Total	1.000	1.012	1.008	1.000	1.002	0.995
CASI01_08 (dense, transl. trees, white background)	Sunlit tree	0.249	0.133	0.868	0.208	<b>0.253</b>	0.279
	Background	0.491	0.538	0.114	0.531	<b>0.367</b>	0.357
	Shadow	0.260	0.319	0.017	0.259	<b>0.379</b>	0.362
	Total	1.000	0.990	0.999	0.998	0.999	0.998
CASI01_09 (sparse, opaque trees, dark background)	Sunlit tree	0.129	0.094	0.270	0.097	<b>0.110</b>	0.109
	Background	0.737	0.707	0.593	<b>0.729</b>	0.734	0.723
	Shadow	0.134	0.189	0.146	0.153	<b>0.154</b>	0.167
	Total	1.000	0.990	1.009	0.979	0.998	0.999
CASI01_10 (sparse, dark background)	Sunlit tree	0.081	0.080	0.830	0.093	<b>0.119</b>	0.104
	Background	0.815	0.625	0.139	0.804	<b>0.738</b>	0.701
	Shadow	0.104	<b>0.215</b>	0.030	0.103	0.142	0.194
	Total	1.000	0.920	0.999	1.000	0.999	0.999
CASI01_11 (dense, opaque trees, white background)	Sunlit tree	0.349	0.271	0.214	0.261	<b>0.296</b>	0.294
	Background	0.390	0.332	0.561	0.388	<b>0.386</b>	0.383
	Shadow	0.261	0.390	0.221	0.291	<b>0.293</b>	0.318
	Total	1.000	0.993	0.996	0.940	0.975	0.995
CASI01_12 (dense, transl. trees, dark background)	Sunlit tree	0.167	0.209	0.163	0.151	<b>0.253</b>	0.279
	Background	0.507	0.383	0.694	0.657	<b>0.371</b>	0.357
	Shadow	0.326	0.429	0.140	0.191	<b>0.387</b>	0.362
	Total	1.000	1.021	0.997	0.999	1.011	0.998

and dense population, the multiple scattering between crowns and the background was more significant but could be accurately modeled by the MLP trained using MTA.

We emphasize that the fractional abundance estimations provided by all MLP-based models were not constrained to be positive or to sum to unity for each pixel. However, negative and/or unrealistic abundance fractions, which usually indicate

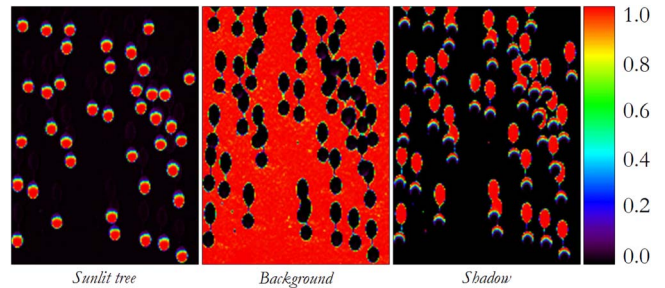


Fig. 4. Endmember fractional abundance maps for sunlit tree, background, and shadow, estimated from the CASI01\_05 scene by our proposed method.

a bad fit of the model and/or reveal inappropriate endmember selections, were very rarely found, in particular, when the MLP was trained using MTA (see Table I).

### V. RESULTS USING REAL AIRBORNE DATA

The image data used in experiments (available in reflectance units) is formed by a ROSIS scene collected at high spatial resolution, with 1.2-m pixels, and its corresponding DAIS scene, collected at low spatial resolution with 6-m pixels. The spectral range from 504–864 nm (covered by the two considered sensors through narrow spectral bands) was selected for experiments. Fig. 5(a) shows the selected test site (located in Caceres, Spain) which contains several cork-oak trees (appearing as dark spots) and pasture (gray) areas on a bare soil (white) background. To obtain reliable estimates of the fractional land covers for each DAIS pixel, the ROSIS image was first classified into the three land-cover components using a maximum-likelihood supervised classification approach based on three image-derived spectral endmembers extracted using the N-FINDR algorithm and shown in Fig. 5(b). Our assumption was that the pixels in the ROSIS image were sufficiently small to become spectrally simple to analyze. Second, the classified ROSIS image was registered with the DAIS image using an automated ground control point-based method with subpixel accuracy. Third, the classification map was associated with the DAIS image to provide an initial estimation of land cover classes for each pixel at the DAIS image scale. For that purpose, a 6 × 6 m grid was overlaid on the 1.2 × 1.2 m classification map derived from the ROSIS scene, where the geographic coordinates of each pixel center point were used to validate the registration procedure at a subpixel level. Then, fractional abundances were calculated within each 6 × 6 m grid as the proportion of ROSIS pixels labeled as cork-oak tree, pasture, and soil within that grid. Most importantly, the abundance maps at the ROSIS level were

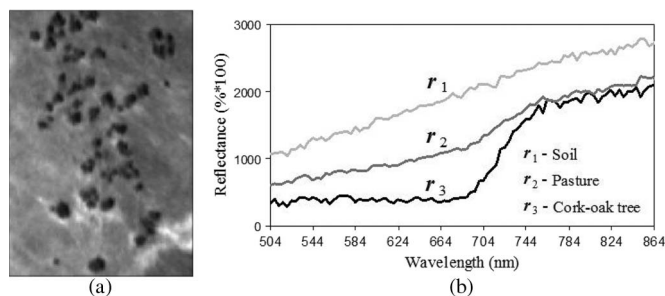


Fig. 5. (a) Band (584 nm) of ROSIS hyperspectral image. (b) Spectral signatures of soil ( $r_1$ ), pasture ( $r_2$ ), cork-oak tree ( $r_3$ ) extracted by N-FINDR.

TABLE II  
NRMSE SCORES (IN PERCENT) IN FRACTIONAL ABUNDANCE ESTIMATION OF SOIL ( $r_1$ ), PASTURE ( $r_2$ ), AND CORK-OAK TREE ( $r_3$ ) IN THE DAIS 7915 IMAGE

Training	Material	Number of training samples ( $k$ )					
		1	2	3	4	5	6
MLP (random)	$r_1$	11.16	11.23	10.84	10.95	10.67	10.58
	$r_2$	15.10	14.49	14.32	13.79	13.62	12.88
	$r_3$	16.26	15.80	15.73	15.21	14.49	13.56
MLP (MTA)	$r_1$	10.04	9.12	6.35	5.66	5.47	5.53
	$r_2$	11.17	8.23	4.39	3.96	4.12	4.03
	$r_3$	14.21	11.35	6.13	6.09	5.95	5.86

refined using GPS-guided field assessment before obtaining a set of reference fractional abundances for each DAIS pixel.

We first measured the normalized root-mean-square error (NRMSE) in the fractional abundance estimation results provided by UCLSU and FCLSU for each of the three pure spectral components shown in Fig. 5(b) with regard to their corresponding reference fractional abundances. In all cases, the NRMSE scores in abundance estimation for the soil ( $r_1$ ), pasture ( $r_2$ ) and cork-oak ( $r_3$ ) were above 10% estimation error in percentage, which suggested that linear mixture modeling was not flexible enough to accommodate the full range of spectral variability throughout the landscape. Table II quantitatively compares the performance of the proposed MLP-based model trained using different algorithms and various numbers of labeled samples (the MLP trained using N-FINDR is not displayed since it provided very similar results to those found by UCLSU). When  $k = 3$  MTA-labeled samples were used in addition to  $p = 3$  endmembers, a significant improvement in abundance estimation was observed with regard to the case in which a higher number of randomly selected training samples were used, with NRMSE scores below 10% in all cases. Interestingly, using additional MTA-labeled training samples did not significantly improve the quality of abundance estimations, thus indicating that the first MTA-labeled samples were the most informative ones. Our Matlab implementation of MTA took only a couple of minutes to extract  $k = 6$  training samples from the ROSIS scene in a dual-core Intel Xeon processor at 2.33 GHz with 3 GB of RAM (the training algorithm took above 40 m of computation in the same environment).

### VI. CONCLUSION AND FUTURE WORK

In this letter, we have experimentally demonstrated that a simple MLP-based neural network architecture, trained using samples intelligently selected by our proposed MTA algorithm,

can improve the fractional abundance estimation results provided by both UCLSU and FCLSU. In a previous study [19], a linear support vector machine (SVM) technique for fractional abundance estimation provided similar results to those found by linear unmixing methods. Since SVMs have great potential for characterization of nonlinear mixtures, further SVM formulations for solving the nonlinear unmixing problem are expected.

### ACKNOWLEDGMENT

The authors thank B. Hu and J. R. Miller for sharing the CASI data sets. Funding from AYA2008-05965-C04-02 and PRI09A110 projects is also gratefully acknowledged.

### REFERENCES

- [1] J. B. Adams, M. O. Smith, and P. E. Johnson, "Spectral mixture modeling: A new analysis of rock and soil types at the Viking Lander 1 site," *J. Geophys. Res.*, vol. 91, no. B8, pp. 8098–8112, Jul. 1986.
- [2] A. Plaza, P. Martinez, R. Perez, and J. Plaza, "A quantitative and comparative analysis of endmember algorithms from hyperspectral data," *IEEE Trans. Geosci. Remote Sens.*, vol. 42, no. 3, pp. 650–663, Mar. 2004.
- [3] N. Keshava and J. F. Mustard, "Spectral unmixing," *IEEE Signal Process. Mag.*, vol. 19, no. 1, pp. 44–57, Jan. 2002.
- [4] D. Heinz and C.-I. Chang, "Fully constrained least squares linear mixture analysis for material quantification in hyperspectral imagery," *IEEE Trans. Geosci. Remote Sens.*, vol. 39, no. 3, pp. 529–545, Mar. 2001.
- [5] J. Plaza, A. Plaza, P. Martinez, and R. Perez, "Joint linear/nonlinear spectral unmixing of hyperspectral image data," in *Proc. IEEE Int. Geosci. Remote Sens. Symp.*, 2007, vol. 1, pp. 4037–4040.
- [6] K. J. Guilfoyle, M. L. Althouse, and C.-I. Chang, "A quantitative and comparative analysis of linear and nonlinear spectral mixture models using radial basis function neural networks," *IEEE Trans. Geosci. Remote Sens.*, vol. 39, no. 10, pp. 2314–2318, Oct. 2001.
- [7] W. Liu and E. Y. Wu, "Comparison of non-linear mixture models," *Remote Sens. Environ.*, vol. 18, pp. 1976–2003, 2004.
- [8] C. C. Borel and S. A. W. Gersl, "Nonlinear spectral mixing models for vegetative and soil surfaces," *Remote Sens. Environ.*, vol. 47, no. 3, pp. 403–416, Mar. 1994.
- [9] N. S. Goel and R. L. Thompson, "A snapshot of canopy reflectance models and a universal model for the radiation regime," *Remote Sens. Rev.*, vol. 18, no. 2–4, pp. 197–225, 2000.
- [10] C. M. Bishop, *Neural Networks for Pattern Recognition*. Oxford, U.K.: Oxford Univ. Press, 1995.
- [11] A. Baraldi, E. Binaghi, P. Blonda, P. A. Brivio, and P. Rampini, "Comparison of the multilayer perceptron with neuro-fuzzy techniques in the estimation of cover class mixture in remotely sensed data," *IEEE Trans. Geosci. Remote Sens.*, vol. 39, no. 5, pp. 994–1005, May 2001.
- [12] M. Chi and L. Bruzzone, "A semilabeled-sample-driven bagging technique for ill-posed classification problems," *IEEE Geosci. Remote Sens. Lett.*, vol. 2, no. 1, pp. 69–73, Jan. 2005.
- [13] B. Hu, J. R. Miller, J. Wang, and N. S. Goel, "Investigation of linear spectral mixtures of the reflectance spectra using laboratory simulated forest scenes," in *Proc. IEEE Int. Geosci. Remote Sens. Symp.*, vol. 3, 2002, pp. 1535–1537.
- [14] C.-I. Chang and Q. Du, "Estimation of number of spectrally distinct signal sources in hyperspectral imagery," *IEEE Trans. Geosci. Remote Sens.*, vol. 42, no. 3, pp. 608–619, Mar. 2004.
- [15] A. Vehtari and J. Lampinen, "Bayesian MLP neural networks for image analysis," *Pattern Recognit. Lett.*, vol. 21, no. 13/14, pp. 1183–1191, Dec. 2000.
- [16] X. Zhuang, B. A. Engel, D. F. Lozano, R. B. Fernández, and C. J. Johansen, "Optimization of training data required for neuro-classification," *Int. J. Remote Sens.*, vol. 15, no. 16, pp. 3271–3277, Nov. 1999.
- [17] G. M. Foody, "The significance of border training patterns in classification by a feedforward neural network using back propagation learning," *Int. J. Remote Sens.*, vol. 20, no. 18, pp. 3549–3562, Dec. 1999.
- [18] M. E. Winter, "N-FINDR: An algorithm for fast autonomous spectral endmember determination in hyperspectral data," *Proc. SPIE*, vol. 3753, pp. 266–277, Oct. 1999.
- [19] J. Plaza, A. Plaza, P. Martinez, and R. Perez, "Nonlinear mixture models for analyzing laboratory simulated-forest hyperspectral data," *Proc. SPIE*, vol. 5508, pp. 660–670, 2003.